Carbon 147 (2019) 594–601

Contents lists available at ScienceDirect

Carbon

journal homepage: www.elsevier.com/locate/carbon

Mechanical responses of boron-doped monolayer graphene

Zhaohe Dai [a, c, 1], Guorui Wang [a, 1], Zhiyue Zheng [d], Yanlei Wang [e, g], Shuai Zhang [e], Xiaoying Qi [a], Pingheng Tan [f], Luqi Liu [a, *], Zhiping Xu [e], Qunyang Li [e], Zhihai Cheng [b, d, **], Zhong Zhang [a, ***]

[a] CAS Key Laboratory of Nanosystem and Hierarchical Fabrication, CAS Center for Excellence in Nanoscience, National Center for Nanoscience and Technology, Beijing, 100190, PR China
[b] Department of Physics and Beijing Key Laboratory of Optoelectronic Functional Materials & Micro-nano Devices, Renmin University of China, Beijing, 100872, PR China
[c] Center for Mechanics of Solids, Structures and Materials, Department of Aerospace Engineering and Engineering Mechanics, The University of Texas at Austin, Austin, TX, 78712, USA
[d] CAS Key Laboratory of Standardization and Measurement for Nanotechnology, CAS Center for Excellence in Nanoscience, National Center for Nanoscience and Technology, Beijing, 100190, PR China
[e] Applied Mechanics Laboratory, Department of Engineering Mechanics and Center for Nano and Micro Mechanics, Tsinghua University, Beijing, 100084, PR China
[f] State Key Laboratory of Superlattices and Microstructures, Institute of Semiconductors, Chinese Academy of Sciences, Beijing, 100083, PR China
[g] State Key Laboratory of Multiphase Complex Systems, Beijing Key Laboratory of Ionic Liquids Clean Process, Institute of Process Engineering, Chinese Academy of Sciences, Beijing, 100190, PR China

ARTICLE INFO

Article history:
Received 19 November 2018
Received in revised form
6 March 2019
Accepted 7 March 2019
Available online 14 March 2019

ABSTRACT

Though pristine graphene exhibits remarkable mechanical and electronic properties, many electromechanical applications may come from chemically doping it with heteroatoms. The goal is to tune the atomic lattice and, in turn, modulate the electronic band structure of graphene – that may also affect the mechanical responses of the graphene sheet. Particularly essential for both practical applications and fundamental interests is to characterize the effect of chemical doping on the mechanical properties of graphene. Here we report graphene can maintain a large fraction of its pristine strength and stiffness after substituting boron for carbon atoms. Counter-intuitively, boron doping can ameliorate the brittle nature of the original lattice by deflecting the cracks and enabling damage-tolerant behaviors. We further offer a direct mapping between the Raman spectra and the measured mechanical performances that can show the relationship between doping structure and mechanical properties of graphene. This work offers important implications for the rational design of graphene-based systems that require chemical modifications and also utilize the mechanics of graphene.

1. Introduction

Perfect graphene, a pure 2D crystalline membrane of covalently bonded carbon atoms, has exhibited excellent in-plane stiffness, strength and carrier mobility [1,2]. The combination of spectacular mechanical and electronic properties postulates graphene as a good candidate in applications such as flexible electronics and electromechanical devices [3–6]. While graphene has an electronic structure with zero band-gap, of particular importance is to modulate the electronic band structure of graphene without sacrificing its mechanical performance. Chemical doping with heteroatoms is a standard way to introduce impurities in the crystal lattice and then tailor the electronic properties of semiconductors [7,8]. For graphene, doping can also be regarded as a promising tool because of its significant effects on the in-plane structure [9]. For instance, boron is an excellent candidate for substituting carbon atoms that can create 0.5% longer and much weaker B-C bonds (compared with C-C bonds) [10–12]. A few percent of boron

---

* Corresponding author.
** Corresponding author. CAS Key Laboratory of Nanosystem and Hierarchical Fabrication, CAS Center for Excellence in Nanoscience, National Center for Nanoscience and Technology, Beijing 100190, China.
*** Corresponding author.
E-mail addresses: liulq@nanoctr.cn (L. Liu), zhihaicheng@ruc.edu.cn (Z. Cheng), zhong.zhang@nanoctr.cn (Z. Zhang).

[1] Equal contribution.

https://doi.org/10.1016/j.carbon.2019.03.014

substitution was expected to induce p-type doping and a significant reduction in thermal conductivity in graphene [7,12,13]. These facts also raise a fundamental question about the doping effects on the mechanical and electronic properties of graphene that are strongly tied to the lattice structure and are crucial parameters for electromechanical applications [14,15].

Significant progress has been achieved recently in clarifying the doping effects on the electronic properties of graphene, along with developments of synthesis methods, structural characterizations, and a variety of exciting applications [16–18]. However, how the doped graphene mechanically behaves remains largely unexplored though each of these applications implicitly depends on its exceptional mechanical performance for structural robustness and reliability [19–21]. In general, substitutional doping of graphene is a process of introducing impurities (*e.g.* substitutional atoms and vacancies) into an sp^2-hybridized hexagonal network. Such impurities were often treated as an undesirable departure from perfection to engineer the material properties, especially mechanical [22]. Alternatively, the weak sense of substituted bonds can also be treated as point defects, which has proven to be a versatile approach to enhance the toughness of traditional materials (*e.g.* metals and ceramics) [23], and may toughen 2D materials [24,25]. Mechanical characterizations of chemically doped 2D materials are thus essential both from a fundamental interest in understanding atom-level structure-property relations and from an engineering perspective for reliable applications.

In the present study, we report the first investigation into the effects of boron doping on the mechanical properties and fracture behaviors of graphene. Graphene samples with controlled boron contents are prepared by mechanical cleavage of boron-doped natural graphite. We identify defect features (regarding substitution-dominated and vacancy-dominated types) as well as their defect density by micro-Raman spectroscopy. We then utilize atomic force microscopy (AFM) nanoindentation to quantify the stiffness, strength, and failure indentation displacement of the doped graphene. Our results indicate that graphene can maintain a large fraction of its pristine strength and stiffness after substituting heteroatoms for carbon atoms. Counter-intuitively, in striking contrast with apparent cracks in pristine graphene that spans across micron length, 2D lattice with substituted boron atoms tends to be capable of deflecting the crack propagation.

2. Experimental

2.1. Sample preparation and characterization

Following well-developed methods in literature [15,26], boron doping was achieved by mixing boron oxide with natural graphite and thermally treating the mixture at $2200°C$ for about 2 h in an argon atmosphere. The weight ratio of boron oxide to graphite ranged from 0.5 to 50. The doping type and the boron content in the graphite were evaluated using X-ray photoelectron spectroscopy (XPS, ESCALAB 250Xi). Note that, increasing treatment time may introduce the vacancies into the graphene lattice [26,27]. The powder diffraction patterns of graphite before and after boron doping were obtained by using synchrotron X-ray diffraction (XRD, Rigaku D/max-2500). The Raman spectra of graphite and exfoliated graphene on SiO_2/Si substrate were measured with a Renishaw Raman system, using the 514 nm line of an Ar laser. HRTEM instruments (FEI Tecnai G2 F20 U-TWIN) were used for high-resolution imaging and electron energy loss spectroscopy (EELS) measurement.

For graphene with substitution-dominated defects, we can roughly convert the boron content of boron-doped graphene to the defect density according to the C-C bond length (1.42 Å) and B-C bond length. Previous density functional theory (DFT) results showed that B-C bond length is around 1.50 Å at the boron concentration of 3.125% [11,12] while the scanning tunneling microscopy (STM) measurements give a slightly different value of 1.59 Å [28]. Herein, the bond length of 1.59 Å was adopted because we used the same fabrication method with the STM one. Therefore, in 1 cm^2, the total number of atoms is about 3.0×10^{15} based on the hexagonal crystal structures. At boron content of 0.5%, the boron density is approximately $1.5 \times 10^{13}\ cm^{-2}$. On the other hand, according to Fig. 1c, the I_D/I_G in Stage I can be linearly proportional to the boron content. As a consequence, we can relate the boron density (n_D) to Raman features by n_D ~$3.6 \times 10^{12}\ I_D/I_G\ cm^{-2}$. We note that this rough estimation is to compare with a previously proposed phenomenological model for graphene with point defects, which also demonstrated a linear relation between I_D/I_G and the defect density in graphene: $n_D \sim 7.3 \times 10^9 E_L^4 I_D/I_G$, where E_L is the laser excitation energy of 2.41 eV in this work [29,30]. Although such relation was based on the Raman spectra of ion-bombarded samples, it should also apply for substitutional graphene in the limit of low n_D [30].

2.2. Friction measurements

Asylum Research (AR) Cypher was employed to perform friction and topography measurements in ambient conditions [31]. During the AFM measurements, silicon probes (MikroMasch, CSC37/Al BS) were used with the lateral force constants calibrated by a diamagnetic lateral force calibrator. The mean friction was calculated by calculating the half difference of the trace and retrace lateral force signals, which were obtained on the region of 100 nm × 100 nm under the sliding velocity of 600 nm s^{-1}.

2.3. Nanoindentation tests

An array of circular holes was patterned onto silicon substrates covered with a 300 nm thick SiO_2 layer through photolithography and reactive ion etching. The depth is ~1 μm and the diameter ranges from 0.5 to 1.5 μm. Monolayer graphene was then transferred on the pre-patterned substrates. Using a commercial AFM system (Asylum Research, MFP-3D Infinity), the nanoindentation test was performed on the suspended part of graphene. Before each indentation, the samples were scanned in tapping mode to find graphene sheets fully covering a hole. After scanning, the AFM tip (NanoScience Instruments) was centered in the middle of the circular hole. The force-displacement curves obtained from the AFM nanoindentation test were used to quantitatively determine the mechanical parameters (*e.g.* in-plane stiffness, fracture strength and strain at break) of our samples. Note that previous attempts to obtain reproducible results with standard Si or slender diamond tips failed because the high stiffness of graphene membranes produced tip breaking [2,32]. To solve this issue, as well as to have a constant and well-defined contact geometry, we use commercial tips from NanoScience Instruments with hemispherical geometry and low wear coating of Tungsten carbide with nominal final tip radius of 60 nm (Fig. S6b) [33]. The cantilever spring constant was calibrated by Sader method before every series of testing, ranging from 38 to 40 N/m. All the measurements presented here were obtained at the same loading/unloading rate (300 nm/s). We follow the well-developed strategy of Lee's work to identify the zero displacement point or zero force level [2].

2.4. Molecular dynamic (MD) simulations

We used the LAMMPS package to perform all the MD simulations [34]. In the case of the nanoindentation test, non-periodic

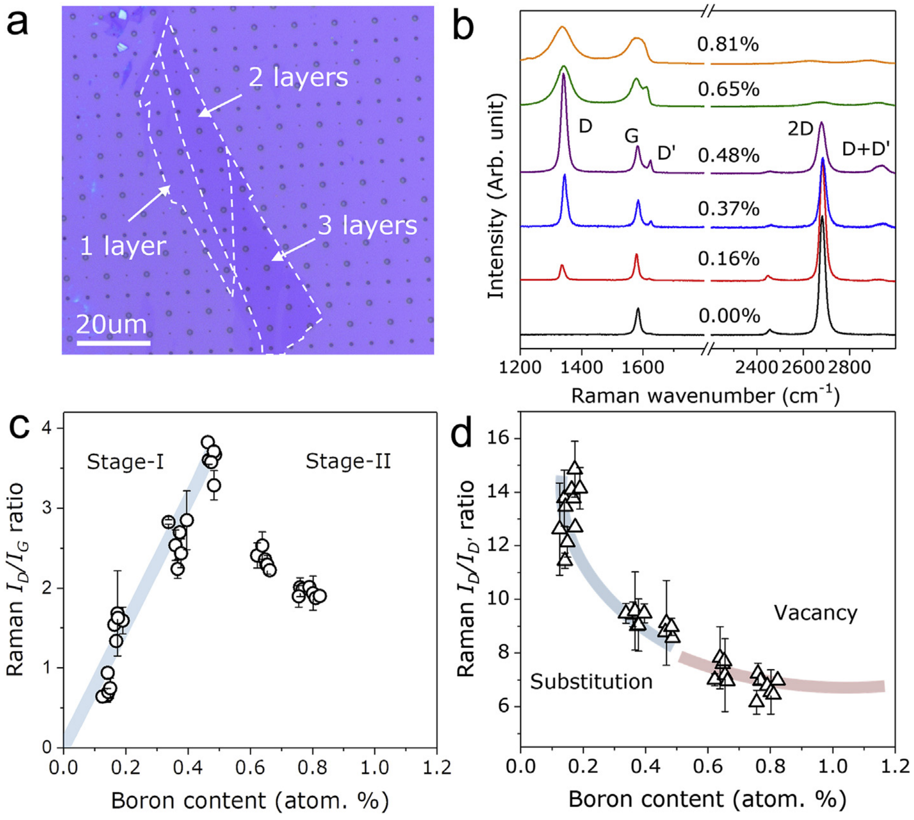

Fig. 1. (a) Optical images of typical graphene sheets including regions of suspended monolayer, bilayer and trilayer graphene. The number of graphene layers was verified with a combination of optical contrast and micro-Raman spectroscopy. (b) Raman spectra of monolayer (1L) graphene with various boron content. (c) I_D/I_G ratio as a function of boron content. The solid blue line is a linear fit for I_D/I_G -boron content relation for the substitution-dominated samples. (d) Raman $I_D/I_{D'}$ ratio as a function of boron, corresponding to a transition from substitution-dominated defect to vacancy-dominated defect. The colored curves are to guide vision. The error bars in y coordinate come from the possible sample differences when those samples are from the same batch made under the same experimental conditions. Note that a few data are not able to include error bars because only one sample was successfully obtained in that case. (A colour version of this figure can be viewed online.)

boundary conditions are applied to the boron-doped graphene, where the shape of boron-doped graphene is a circle with radius $R_G = 15.6$ nm. In the case of tearing test, non-periodic boundary conditions are also used in three directions, and the size of the graphene sheet is 20.70×15.48 nm^2 embedded with a 1.7-nm-long pre-crack in the left edge. The Tersoff potential was used for the interatomic interaction between the carbon atoms and boron atoms in the same layer, which has been used to predict the structural, thermal, and mechanical properties of both carbon and boron nanostructure [35,36]. Note that the Tersoff potential was also used for carbon-nitride interactions [37]. The boron doping and vacancy will distribute randomly in the sheet of graphene, and the concentration is defined as $c_{\text{defect}} = N_B(N_{\text{vac}})/N_C$, where N_B, N_{vac}, and N_C are the number of the boron atom, mono-vacancy and carbon atom in the system. The atomic structure of graphene constructed was optimized using a conjugate-gradient algorithm before mechanical tests were performed. The mechanical responses were investigated by performing MD simulations at 0 K with a timestep of 0.2 fs. The NVE ensemble and Berendsen thermostat were used to maintain the temperature and volume [38]. In nanoindentation simulations, the edges of graphene (the outer ring with a width of 1 nm) were fixed, and a spherical indenter with a radius of 1 nm was used at the center of the membrane. The entire system will be firstly equilibrated for 200 ps. Then the indenter was moved downward with a speed of 1 m/s to introduce the fracture of graphene, which took about 500 ps. The force applied on the indenter was tracked during the indentation simulations as shown in Fig. S8 that also gives rise to the in-plane stiffness or Young's modulus of the graphene (Fig. S9). In the simulation of tearing apart the graphene, a constant velocity ($v = 20$ and -20 m/s) is set to the four rows of atoms at the top and bottom of graphene, respectively, as shown in Fig. S11. The total simulated time for tearing process is about 300 ps.

3. Results and discussion

3.1. Fabrication and characterization of boron-doped graphene

Following the well-established procedure [15,26], boron-doped graphite with a series of boron content was prepared by mixing boron oxide with natural graphite at $2200^\circ C$ (see Method). X-ray photoelectron spectroscopy (XPS) was employed to identify the total boron content in graphite. We then quantify the substitutional doping according to the curve-fitted areas for B1s spectra and found that doping content is less than 1.0%. Through X-ray diffraction (XRD) characterization, we also confirmed subtle structural changes in graphite [27]. Notably, methods based chemical vapor deposition or graphene oxide can dope graphene with relatively high boron contents. However, the resulted samples typically include defects such as grain boundaries, functional groups that make the samples not suitable for mechanical testing purposes [39].

We prepare monolayer and few-layer boron-doped graphene sheets (Fig. 1a) by the mechanical exfoliation of boron-doped graphite. Later in the text, we label the monolayer boron-doped graphene sheet based on the XPS-derived boron content in its host graphite. Owing to the low doping amount and the close atomic size between boron and carbon atoms, we observed negligible differences in the texture between few-layer graphene and boron-doped graphene as characterized by transmission electron microscopy (TEM) (Fig. S2). The presence and the distribution of boron atoms in the doped graphene are further validated by electron energy-loss spectroscopy (EELS) (Fig. S3).

When introducing the boron substitutions, we may also introduce vacancy-type defects in the graphene sheet. Before mechanical tests, we first use micro-Raman spectroscopy to identify which type of defects is dominated in our boron-doped monolayer samples. Fig. 1b shows typical Raman spectra of boron-doped monolayer graphene sheets with different boron contents. Notably, the defect-activated features (D-, D′- and D + D′-band) are visible, in which the I_D/I_G ratio is related to the number of defect sites per unit area, namely defect density [28,40,41]. Fig. 1c shows two-staged, non-monotonic I_D/I_G ratios as functions of the boron content for boron-doped monolayer graphene. Note that the intensity ratios are calculated by deconvolution here that takes the area under the curve as a measurement of the Raman peak intensity. Specifically, at relatively low boron concentration (<0.48%, Stage-I), the I_D/I_G ratio increases with the boron content, featuring characteristic Raman bands for substitution-dominated defects (i.e. relatively sharp D-band and weak D′-band as shown in Fig. 1b). In this case, the boron content follows a simple linear relationship with the I_D/I_G ratio (blue line in Fig. 1c). This observation agrees with previous reports on the linear relation between I_D/I_G ratio and the defect density in graphene (see details in Experimental Section) [30]. However, for monolayer samples exfoliated from graphite with relatively high boron concentration (>0.48%, Stage-II), the I_D/I_G ratio decreases with the boron content as shown in Fig. 1c, along with characteristic Raman bands for vacancy-dominated defects (i.e. relatively broadening D-band and strong D′-band). The Raman peak broadening typically originates from the structural disorders in a lattice structure. Also, slight Raman shifts can also be observed due to the combined effect of the boron-induced shift of Femi energy and tensile strains in graphene lattice. We suggest that the two-staged feature could be a result of a transition from substitution-dominated to vacancy-dominated defect type when doping graphene sheets. Note that this transition was also observed when oxidizing graphene sheets [42].

We further plot the $I_D/I_{D'}$ ratio as a function of the boron content in Fig. 1d. $I_D/I_{D'} = 11.5 \pm 2.5$ may relate to the substitution-dominated domain and $I_D/I_{D'} = 7.5 \pm 2.2$ may relate to the vacancy-dominated domain. We find that these values are consistent with previous works: $I_D/I_{D'} \approx 13$ for substitutional boron and $I_D/I_{D'} \approx 7$ for vacancies [40,43]. Meanwhile, the full width at half-maximum of G-band (Γ_G) is also a measure to discriminate such two stages, as samples in Stage-I and -II could have the same I_D/I_G, but different Γ_G (Fig. S4) [33,44]. Additionally, even though we failed at characterizing a detailed portion of defect types based on high-resolution TEM or scanning tunneling microscopy, we employed friction force microscopy (Fig. S5) to show discernible differences in atomic lattices for pristine, substitution-dominated, and vacancy-dominated graphene samples at a nanometer scale [45,46].

3.2. Nanoindentation tests

We then study the effects of boron doping on the mechanical properties of monolayer graphene. We prepared a series of samples and identified their defect types by micro-Raman spectroscopy as mentioned above. The same method has been involved in characterizing the defect types of coupled-plasma-treated graphene samples in Eckmann's work [43]. Suspended graphene flakes were prepared on pre-patterned silicon substrates (an array of circular holes by photolithography and reactive ion etching) as shown in Figs. 1a and S6a. We then use an AFM tip to indent the graphene membranes at the center of the suspended area as reported previously (Fig. 2a) [33,47]. We used commercially available tips here with hemispherical geometry (radius: 60 nm) and low wear coating.

Fig. 2b shows typical force-displacement curves for pristine monolayer graphene (P-graphene) and boron-doped monolayer graphene (B-graphene) with substitution- and vacancy-dominated defects. This indentation process was modeled as clamped circular membranes with a central point loading, which offered Equation (1) consisting of a linear and cubic deflection term to determine in-plane elastic modulus E_{2D}:

$$F(\delta) = \pi\sigma_0\delta + E_{2D}\delta^3 \Big/ a^2 \tag{1}$$

where F is the loading force, δ is the indentation displacement at the central point, a is the radius of patterned holes and σ_0 is the pretension accumulated in the sheets since slight, uncontrollable initial deflection (−5 to +5 nm) could be observed usually. For P-graphene, this equation could fit its force-displacement curves very well in Fig. 2b (blue line), because the most area of the suspended graphene is constrained within linear stress-strain relation during the indentation process (even till fracture) [2]. Results obtained in up to 30 pristine drumheads yielded values of E_{2D} in 329 ± 40 N/m, in good agreement with previous reports [2,33,42].

The linear elastic behavior of P-graphene also led to a nearly constant slope for its force-cubed displacement curve in Fig. 2c, implying the constant in-plane stiffness E_{2D} of thin membranes. In fact, the slope shows a subtle transition at small indentation displacement (0.1–10 nm) in Fig. 2c inset and then the cubic term in Equation (1) gradually dominates. Such transition starts coincidentally at a length scale defined by the ratio between the bending stiffness and the in-plane stiffness [48]. Interestingly, for boron-doped graphene, Equation (1) cannot offer good fitting in Fig. 2b, and the slope in Fig. 2d varies throughout the indentation process (red and green markers). This implies that both the substitution- and vacancy-dominated defects could affect the mechanical response of the in-plane hexagonal lattice structure of graphene. Such nonlinear behavior may come from the nonlinear properties of the doped material or doping-caused geometrical distortion, calling for further studies both experimentally and theoretically. For example, one possible explanation is the formation of sp^3 carbon (according to the C1s peak fitting in Fig. S1) in doped samples. According to the strategies for measuring Young's modulus of nonlinear materials [49,50], in the following discussions, we determine E_{2D} of B-graphene based on the fitting results within initial indentation displacement (i.e. 50 nm) as illustrated in Fig. 2b.

Of particular interests is the evolution of the 2D elastic modulus (E_{2D}) with the defect type and content (Fig. 3a). Notably, E_{2D} remains its defect-free value over the substitution-dominated region (until boron content of 0.48%), indicating that these substitution-induced defects do not appreciably change the stiffness. However, once the defect type in doped graphene crosses over into the vacancy-dominated region (boron content > 0.48%), we observed significant decreases of E_{2D} with increasing boron content. Individually, at the boron content of around 0.81%, vacancy-dominated graphene can sustain 60% of the original stiffness for the graphene sheet.

Unlike the elastic stiffness, the strength (σ_{2D}) is more sensitive to defects regardless of their types. Typically, σ_{2D} was derived from the maximum indenting force the graphene can undergo before breaking via an approximate model $\sigma_{2D} = \sqrt{F_{break}E_{2D}/4\pi R}$

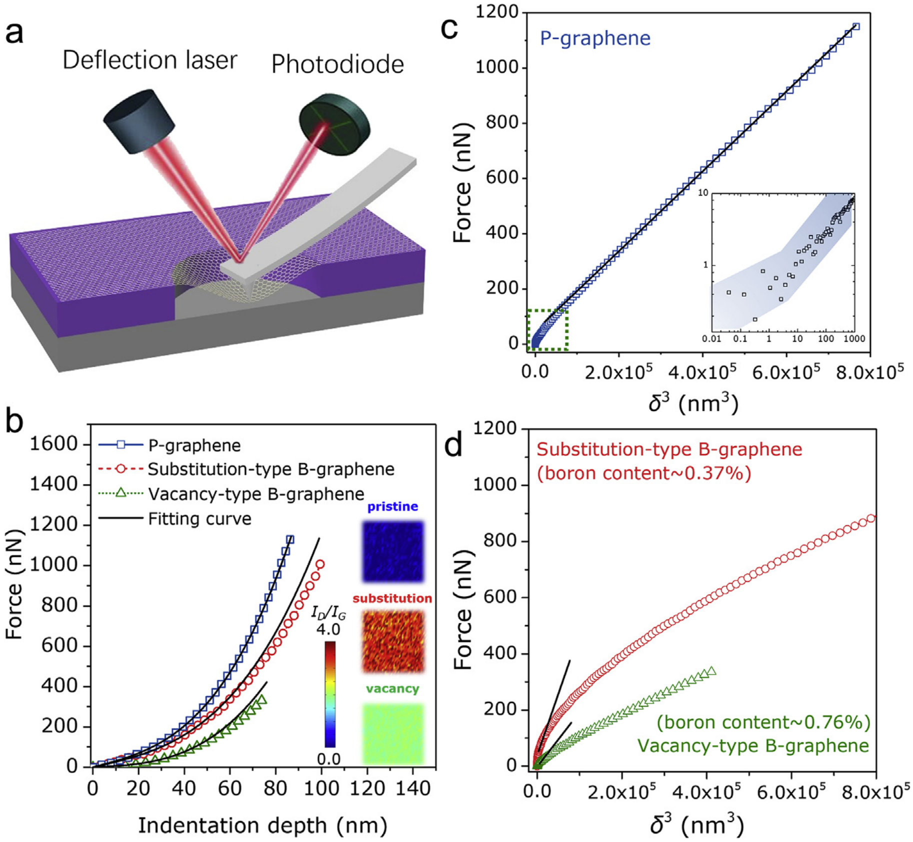

Fig. 2. (a) Schematic representation of the AFM nanoindentation test on suspended samples. (b) Typical force-displacement curves for pristine graphene (P-graphene, blue) and boron-doped graphene (B-graphene) with substitution- (red, boron content: 0.37%) and vacancy-dominated defects (green, boron content: 0.76%). (c) Indentation force as a function of the cubed indentation displacement for pristine graphene. The inset shows zoom-in data to highlight the initial indentation process. (d) Nonlinearity in the force-displacement relation for both substitution- (red) and vacancy-dominated (green) doped graphene. Black solid lines are linearly labeled. (A colour version of this figure can be viewed online.)

(Fig. 3b), where F_{break} is the breaking force in our nanoindentation tests and R is the tip radius. While this model slightly overestimates the strength because of the nonlinear elasticity of 2D lattice when approaching fracture, it has been widely used in the literature and allows comparative studies [33,47]. We hence roughly estimate the strength of all sample following this oversimplified model here, which yields 45 ± 7 N/m for pristine graphene. This value is consistent with previous measurements on pristine graphene [2,33,42]. The breaking strength could remain 80% (*i.e.* 36 ± 4 N/m) for boron-doped graphene with a substitutional boron content of 0.48%, and then dropped precipitously in the vacancy-dominated regime. The evolution of modulus and strength with defects in this work is in good agreement with recent elegant works by Zandiatashbar et al. where oxygen-etching monolayer graphene was tested by nanoindentation [42]. Specifically, the elastic modulus and strength of oxidized graphene are relatively insensitive to sp^3-type defects. By contrast, the mechanical properties of oxidized graphene degrade significantly when the oxygen caused vacancy-type defects.

Interestingly, in contrast to the reduction in strength, a counter-intuitive increment in the maximum indentation (failure) displacement is observed with increasing substitution density (Fig. 3c). Even at the vacancy-dominated regime, the failure displacement of defective graphene is also comparable to that of pristine sheets. One possible reason is that the presence of defects in graphene can localize cracks and extend the maximum deformation before failure, which may be analogous to A4 papers with patterned holes. These results have important practical implications for the design of a broad range of graphene-based applications, where the extraordinary mechanical performances are essential, and the emergence of chemical modifications and substitution is inevitable [51–53]. Also, using the direct mapping between the Raman parameters and the measured stiffness and strength in Figs. 2 and 3, it is highly possible to determine how the mechanical properties of graphene vary as a function of doping/defect density in a quantitative yet non-destructive manner.

3.3. *Fracture behaviors of boron-doped graphene*

Having shown the effect of boron doping on the structural defects, as well as stiffness, strength and failure displacement of graphene sheets, we further observe the morphology of our tested samples after being penetrated by indentation tips. Fig. 4a–c displays representative SEM images of fractured pristine, substitution-dominated and vacancy-dominated graphene, respectively. Consistent with previously reported brittleness of graphene [24,25], pristine membranes showed large-area tears with ~30% residual area in the hole according to observations of 23 samples, as shown in Figs. 4d and S7a. Interestingly, by contrast, boron-substituted membranes showed a markedly different behavior — localized failure mode rather than a catastrophic failure in Fig. 4b with ~70% residual area (Figs. 4e and S7b). Our results imply that the presence of weak B-C bonds substantially deflects crack propagation and effectively prevents the crack tip from spanning the entire membrane. Similar localized fractures were also reported for argon ions irradiated graphene with a random distribution of mono-vacancies [47]. In striking contrast, multi-vacancies with larger voids tend to be formed by doping reaction, leading to brittle

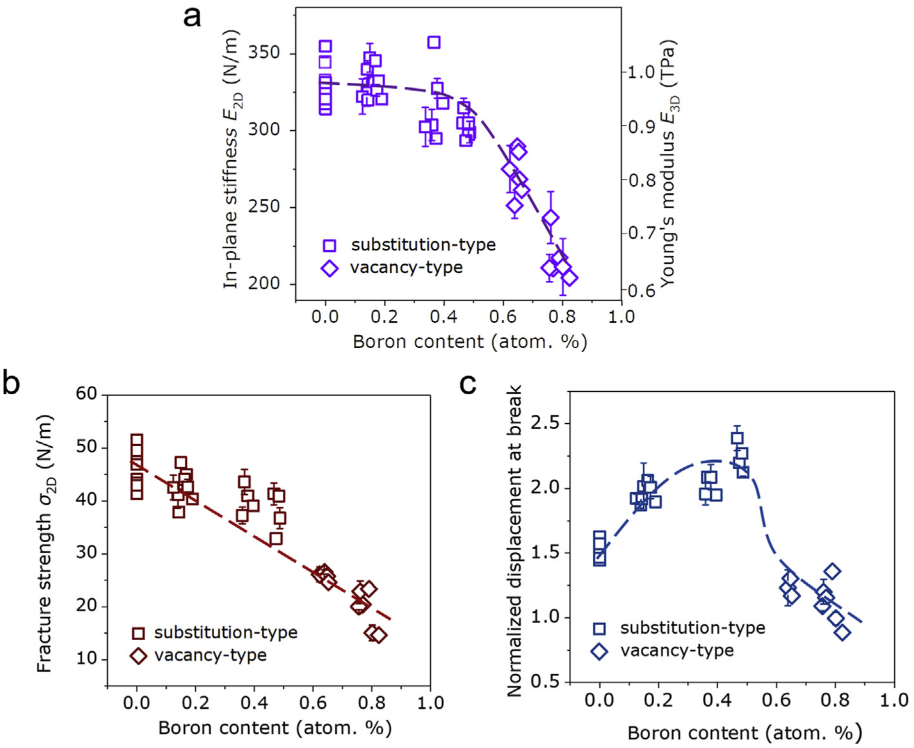

Fig. 3. Experimental results of (a) E_{2D}, (b) σ_{2D} and (c) normalized break displacement of graphene as a function of boron content. The break displacement is normalized by the radius of the hole in (c), and we only showed tests performed on 1.0-μm holes. Part of data in a-c shows error bars in *y* coordinate because these samples can cover more than one holes such that we can perform multiple indentation tests on different holes and then make the statistics. (A colour version of this figure can be viewed online.)

behaviors (Fig. 4c). The suspended area is even less than 20% as shown in Figs. 4f and S7c. These results include one of our central findings: graphene can maintain a large fraction of its pristine strength and stiffness and even behaves more damage-tolerant, after substituting heteroatoms for carbon atoms. One can balance this relation between chemical modifications/substitutions and stiffness, failure strength as well as ductility of the material for the rational design of graphene-based materials in the future.

The underlying mechanism is elucidated by MD simulations regarding how defects affect the mechanical responses of graphene in the nanoindentation tests. For graphene, it can be envisioned that the cracks mainly run along the zigzag directions due to their lower formation energy. To reveal the experimentally observed fracture behavior for boron-doped graphene, we hence focus on the effects of defect on the formation energy (E_F), which defines how difficult a crack grows in a specific direction. As shown in Fig. S10, the substitution-dominated defect tends to reduce the formation energy of the armchair edge, while enhancing that of the zigzag edge. In other words, the crack in graphene with the substitution-dominated defects can grow randomly with torn edges aligned with either armchair or zigzag directions. This may eventually form a confined fracture region as we observed in Fig. 4. However, the vacancy-dominated defect will increase the formation energy of both armchair and zigzag edges and the cracks again prefer the zigzag direction. In addition, when the cracks further propagate to a larger area, a chain reaction between adjacent vacancy defects occurs that causes extensive structural damages.

To gain further insights into the dynamic process of crack propagation in different structures excluding the geometric effect, we performed additional MD simulations of the in-plane fracture on larger scales as shown in Fig. S11. As expected, the evolution of cracks and characteristics of torn edges for graphene with three different structures are analogous to the results as discussed above (Fig. S12). Comparing with the sharp (zigzag) edges observed in pristine graphene and vacancy-dominated graphene, substitution-dominated graphene tends to exhibit relatively smooth crack tips (mix of zigzag and armchair edges). In addition to the crack branching effect, the substitutional boron atoms also slow down the crack growth in graphene. Through the calculation of the total time consumed for the formation of the full crack across the length, the growth rate is merely ~53 nm/ps for substitution-dominated graphene, which is nearly one-third of that for pristine graphene (~152 nm/ps). The slowed down crack propagation is anticipated to enhance the ability of graphene to resist the catastrophic fracture.

4. Conclusion

In summary, we highlight the mechanical performance of boron-doped graphene with substitution-dominated defects. The stiffness and strength of graphene are relatively insensitive to the atom substitution even at a concentration of 0.48%, while the failure strain and damage tolerance can even be improved by such defects. These observations have important practical implications for the design of graphene-based devices since heteroatoms doping is essential to modulate the electronic band structure of graphene without significantly sacrificing its mechanical performances. Even at the vacancy-dominated defect regime, graphene can maintain a large fraction of its pristine strength and stiffness. Following our direct mapping between the Raman parameters and the measured mechanical performance here, one may balance relation between 'chemical substitutions and structural vacancy' and 'stiffness, failure strength as well as failure behavior' of graphene. The establishment of this structure-property relationship is also of fundamental importance for the rational design of lattice structures to avoid brittle failure of 2D materials.

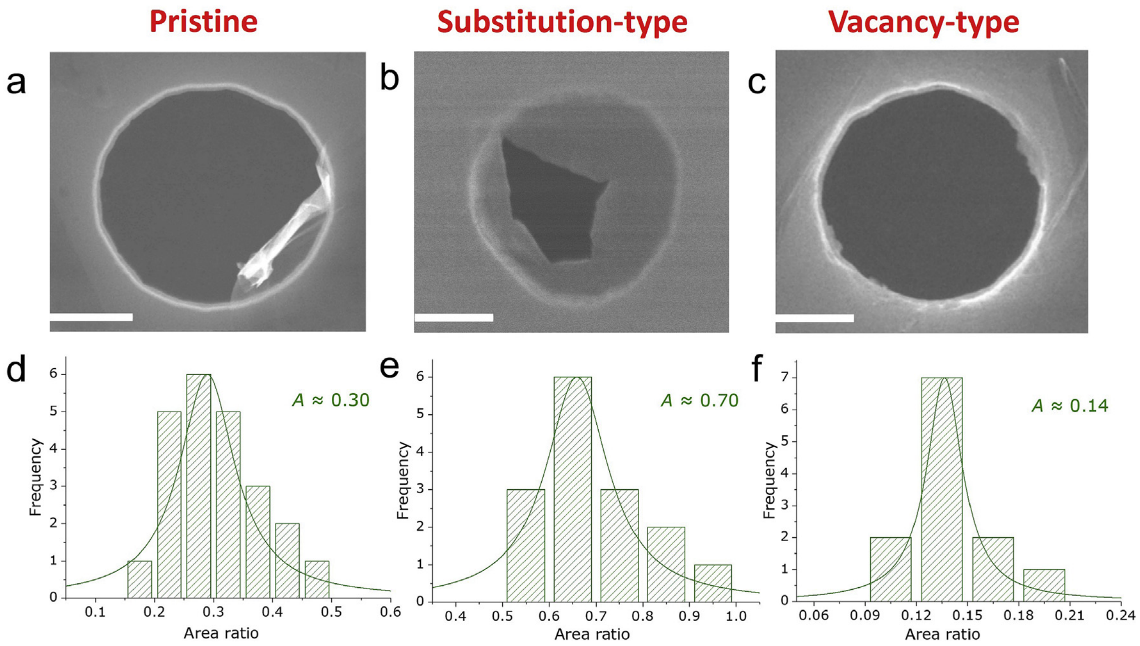

Fig. 4. (a–c) Representative SEM images of graphene drumheads after breaking during indentation experiments. Scale bar is 200 nm. The transition from catastrophic, to localized, to catastrophic failure for (a) P-graphene and B-graphene with (b) substitution- and (c) vacancy-dominated defect. The ratio of the area of remained graphene to the area of the hole (*A*) for (d) P-graphene and B-graphene with (e) substitution- and (f) vacancy-dominated defects, obtained from 23, 15, 12 samples, respectively. (A colour version of this figure can be viewed online.)

Acknowledgements

Z. D. and G. W. contributed equally to this work. This project was jointly supported by the National Key Basic Research Program of China (Grant Nos. 2013CB934203, 2012CB937503 and 2016YFA0200700), the National Natural Science Foundation of China (Grant Nos. 11832010, 11890682, 21474023 and 61674045) and the Beijing Natural Science Foundation (Grant No. 2184124).

Appendix A. Supplementary data

Supplementary data to this article can be found online at https://doi.org/10.1016/j.carbon.2019.03.014.

References

[1] A.C. Neto, F. Guinea, N. Peres, K. Novoselov, A. Geim, The electronic properties of graphene, Rev. Mod. Phys. 81 (1) (2009) 109.
[2] C. Lee, X. Wei, J.W. Kysar, J. Hone, Measurement of the elastic properties and intrinsic strength of monolayer graphene, Science 321 (5887) (2008) 385–388.
[3] J.D. Shi, X.M. Li, H.Y. Cheng, Z.J. Liu, L.Y. Zhao, T.T. Yang, Z.H. Dai, Z.G. Cheng, E.Z. Shi, L. Yang, Z. Zhang, A.Y. Cao, H.W. Zhu, Y. Fang, Graphene reinforced carbon nanotube networks for wearable strain sensors, Adv. Funct. Mater. 26 (13) (2016) 2078–2084.
[4] D. Akinwande, N. Petrone, J. Hone, Two-dimensional flexible nanoelectronics, Nat. Commun. 5 (2014) 5678.
[5] Z.H. Dai, Y.L. Wang, L.Q. Liu, X.L. Liu, P.H. Tan, Z.P. Xu, J. Kuang, Q. Liu, J. Lou, Z. Zhang, Hierarchical graphene-based films with dynamic self-stiffening for biomimetic artificial muscle, Adv. Funct. Mater. 26 (38) (2016) 7003–7010.
[6] Z. Dai, L. Liu, Z. Zhang, Strain engineering of 2D materials: issues and opportunities at the interface, Adv. Mater. (2019) 1805417, https://doi.org/10.1002/adma.201805417.
[7] D.Y. Usachov, A.V. Fedorov, O.Y. Vilkov, A.E. Petukhov, A.G. Rybkin, A. Ernst, M.M. Otrokov, E.V. Chulkov, I.I. Ogorodnikov, M.V. Kuznetsov, Large-scale sublattice asymmetry in pure and boron-doped graphene, Nano Lett. 16 (7) (2016) 4535–4543.
[8] G. Giovannetti, P. Khomyakov, G. Brocks, V.v. Karpan, J. Van den Brink, P.J. Kelly, Doping graphene with metal contacts, Phys. Rev. Lett. 101 (2) (2008) 026803.
[9] L. Panchakarla, A. Govindaraj, C. Rao, Boron-and nitrogen-doped carbon nanotubes and graphene, Inorg. Chim. Acta 363 (15) (2010) 4163–4174.
[10] L. Ci, L. Song, C. Jin, D. Jariwala, D. Wu, Y. Li, A. Srivastava, Z. Wang, K. Storr, L. Balicas, Atomic layers of hybridized boron nitride and graphene domains, Nat. Mater. 9 (5) (2010) 430.
[11] S. Ullah, A. Hussain, W. Syed, M.A. Saqlain, I. Ahmad, O. Leenaerts, A. Karim, Band-gap tuning of graphene by Be doping and Be, B co-doping: a DFT study, RSC Adv. 5 (69) (2015) 55762–55773.
[12] S. Ullah, A. Hussain, F. Sato, Rectangular and hexagonal doping of graphene with B, N, and O: a DFT study, RSC Adv. 7 (26) (2017) 16064–16068.
[13] B. Mortazavi, S. Ahzi, Molecular dynamics study on the thermal conductivity and mechanical properties of boron doped graphene, Solid State Commun. 152 (15) (2012) 1503–1507.
[14] Z. Dai, Y. Hou, D.A. Sanchez, G. Wang, C.J. Brennan, Z. Zhang, L. Liu, N. Lu, Interface governed deformation of nanobubbles and nanotents formed by two-dimensional materials, Phys. Rev. Lett. 121 (26) (2018) 266101.
[15] Y.A. Kim, K. Fujisawa, H. Muramatsu, T. Hayashi, M. Endo, T. Fujimori, K. Kaneko, M. Terrones, J. Behrends, A. Eckmann, C. Casiraghi, K.S. Novoselov, R. Saito, M.S. Dresselhaus, Raman spectroscopy of boron-doped single-layer graphene, ACS Nano 6 (7) (2012) 6293–6300.
[16] F. Banhart, J. Kotakoski, A.V. Krasheninnikov, Structural defects in graphene, ACS Nano 5 (1) (2010) 26–41.
[17] L. Panchakarla, K. Subrahmanyam, S. Saha, A. Govindaraj, H. Krishnamurthy, U. Waghmare, C. Rao, Synthesis, structure, and properties of boron-and nitrogen-doped graphene, Adv. Mater. 21 (46) (2009) 4726–4730.
[18] Z. Peng, R. Ye, J.A. Mann, D. Zakhidov, Y. Li, P.R. Smalley, J. Lin, J.M. Tour, Flexible boron-doped laser-induced graphene microsupercapacitors, ACS Nano 9 (6) (2015) 5868–5875.
[19] A. Shekhawat, R.O. Ritchie, Toughness and strength of nanocrystalline graphene, Nat. Commun. 7 (2016) 10546.
[20] D.A. Sanchez, Z. Dai, P. Wang, A. Cantu-Chavez, C.J. Brennan, R. Huang, N. Lu, Mechanics of spontaneously formed nanoblisters trapped by transferred 2D crystals, Proc. Natl. Acad. Sci. Unit. States Am. 115 (31) (2018) 7884–7889.
[21] G. Wang, Z. Dai, Y. Wang, P. Tan, L. Liu, Z. Xu, Y. Wei, R. Huang, Z. Zhang, Measuring interlayer shear stress in bilayer graphene, Phys. Rev. Lett. 119 (3) (2017) 036101.
[22] D. Akinwande, C.J. Brennan, J.S. Bunch, P. Egberts, J.R. Felts, H. Gao, R. Huang, J.-S. Kim, T. Li, Y. Li, A review on mechanics and mechanical properties of 2D materials—graphene and beyond, Extrem. Mech. Lett. 13 (2017) 42–77.
[23] K. Lu, L. Lu, S. Suresh, Strengthening materials by engineering coherent internal boundaries at the nanoscale, Science 324 (5925) (2009) 349–352.
[24] T. Zhang, H. Gao, Toughening graphene with topological defects: a perspective, J. Appl. Mech. 82 (5) (2015) 051001.
[25] T. Zhang, X. Li, H. Gao, Fracture of graphene: a review, Int. J. Fract. 196 (1–2) (2015) 1–31.
[26] G.R. Wang, X.L. Li, Y.L. Wang, Z.Y. Zheng, Z.H. Dai, X.Y. Qi, L.Q. Liu, Z.H. Cheng, Z.P. Xu, P.H. Tan, Z. Zhang, Interlayer coupling behaviors of boron doped multilayer graphene, J. Phys. Chem. C 121 (46) (2017) 26034–26043.
[27] T. Shirasaki, A. Derré, M. Ménétrier, A. Tressaud, S. Flandrois, Synthesis and

characterization of boron-substituted carbons, Carbon 38 (10) (2000) 1461–1467.
[28] M. Endo, T. Hayashi, S.-H. Hong, T. Enoki, M.S. Dresselhaus, Scanning tunneling microscope study of boron-doped highly oriented pyrolytic graphite, J. Appl. Phys. 90 (11) (2001) 5670–5674.
[29] A.C. Ferrari, Raman spectroscopy of graphene and graphite: disorder, electron–phonon coupling, doping and nonadiabatic effects, Solid State Commun. 143 (1–2) (2007) 47–57.
[30] L.G. Cançado, A. Jorio, E.M. Ferreira, F. Stavale, C. Achete, R. Capaz, M. Moutinho, A. Lombardo, T. Kulmala, A. Ferrari, Quantifying defects in graphene via Raman spectroscopy at different excitation energies, Nano Lett. 11 (8) (2011) 3190–3196.
[31] Q. Li, K.-S. Kim, A. Rydberg, Lateral force calibration of an atomic force microscope with a diamagnetic levitation spring system, Rev. Sci. Instrum. 77 (6) (2006) 065105.
[32] X. Wei, Z. Meng, L. Ruiz, W. Xia, C. Lee, J.W. Kysar, J.C. Hone, S. Keten, H.D. Espinosa, Recoverable slippage mechanism in multilayer graphene leads to repeatable energy dissipation, ACS Nano 10 (2) (2016) 1820–1828.
[33] G. López-Polín, C. Gómez-Navarro, V. Parente, F. Guinea, M.I. Katsnelson, F. Pérez-Murano, J. Gómez-Herrero, Increasing the elastic modulus of graphene by controlled defect creation, Nat. Phys. 11 (1) (2015) 26–31.
[34] S. Plimpton, Fast parallel algorithms for short-range molecular dynamics, J. Comput. Phys. 117 (1) (1995) 1–19.
[35] L. Lindsay, D. Broido, Optimized Tersoff and Brenner empirical potential parameters for lattice dynamics and phonon thermal transport in carbon nanotubes and graphene, Phys. Rev. B 81 (20) (2010) 205441.
[36] A. Kınacı, J.B. Haskins, C. Sevik, T. Çağın, Thermal conductivity of BN-C nanostructures, Phys. Rev. B 86 (11) (2012) 115410.
[37] Y. Dong, M. Meng, M.M. Groves, C. Zhang, J. Lin, Thermal conductivities of two-dimensional graphitic carbon nitrides by molecule dynamics simulation, Int. J. Heat Mass Transf. 123 (2018) 738–746.
[38] H.J. Berendsen, J.v. Postma, W.F. van Gunsteren, A. DiNola, J. Haak, Molecular dynamics with coupling to an external bath, J. Chem. Phys. 81 (8) (1984) 3684–3690.
[39] C. Rao, K. Gopalakrishnan, A. Govindaraj, Synthesis, properties and applications of graphene doped with boron, nitrogen and other elements, Nano Today 9 (3) (2014) 324–343.
[40] A. Eckmann, A. Felten, I. Verzhbitskiy, R. Davey, C. Casiraghi, Raman study on defective graphene: effect of the excitation energy, type, and amount of defects, Phys. Rev. B 88 (3) (2013) 035426.
[41] A.C. Ferrari, D.M. Basko, Raman spectroscopy as a versatile tool for studying the properties of graphene, Nat. Nanotechnol. 8 (4) (2013) 235.
[42] A. Zandiatashbar, G.H. Lee, S.J. An, S. Lee, N. Mathew, M. Terrones, T. Hayashi, C.R. Picu, J. Hone, N. Koratkar, Effect of defects on the intrinsic strength and stiffness of graphene, Nat. Commun. 5 (2014) 3186.
[43] A. Eckmann, A. Felten, A. Mishchenko, L. Britnell, R. Krupke, K.S. Novoselov, C. Casiraghi, Probing the nature of defects in graphene by Raman spectroscopy, Nano Lett. 12 (8) (2012) 3925–3930.
[44] E.M. Ferreira, M.V. Moutinho, F. Stavale, M. Lucchese, R.B. Capaz, C. Achete, A. Jorio, Evolution of the Raman spectra from single-, few-, and many-layer graphene with increasing disorder, Phys. Rev. B 82 (12) (2010) 125429.
[45] T. Filleter, J.L. McChesney, A. Bostwick, E. Rotenberg, K.V. Emtsev, T. Seyller, K. Horn, R. Bennewitz, Friction and dissipation in epitaxial graphene films, Phys. Rev. Lett. 102 (8) (2009) 086102.
[46] C. Lee, Q. Li, W. Kalb, X.-Z. Liu, H. Berger, R.W. Carpick, J. Hone, Frictional characteristics of atomically thin sheets, Science 328 (5974) (2010) 76–80.
[47] G. López-Polín, J. Gómez-Herrero, C. Gómez-Navarro, Confining crack propagation in defective graphene, Nano Lett. 15 (3) (2015) 2050–2054.
[48] K.M. Yue, W. Gao, R. Huang, K.M. Liechti, Analytical methods for the mechanics of graphene bubbles, J. Appl. Phys. 112 (8) (2012) 083512.
[49] R.A. Schapery, On the characterization of nonlinear viscoelastic materials, Polym. Eng. Sci. 9 (4) (1969) 295–310.
[50] Z.H. Dai, Y. Gao, L.Q. Liu, P. Potschke, J.L. Yang, Z. Zhang, Creep-resistant behavior of MWCNT-polycarbonate melt spun nanocomposite fibers at elevated temperature, Polymer 54 (14) (2013) 3723–3729.
[51] X. Wang, X. Li, L. Zhang, Y. Yoon, P.K. Weber, H. Wang, J. Guo, H. Dai, N-doping of graphene through electrothermal reactions with ammonia, Science 324 (5928) (2009) 768–771.
[52] Z. Dai, G. Wang, L. Liu, Y. Hou, Y. Wei, Z. Zhang, Mechanical behavior and properties of hydrogen bonded graphene/polymer nano-interfaces, Compos. Sci. Technol. 136 (2016) 1–9.
[53] G. Wang, Z. Dai, L. Liu, H. Hu, Q. Dai, Z. Zhang, Tuning the interfacial mechanical behaviors of monolayer graphene/PMMA nanocomposites, ACS Appl. Mater. Interfaces 8 (34) (2016) 22554–22562.